

Depth-Assisted Network for Indiscernible Marine Object Counting with Adaptive Motion-Differentiated Feature Encoding

Chengzhi Ma, Kunqian Li, *Member, IEEE*, Shuaixin Liu, and Han Mei

Abstract—Indiscernible marine object counting encounters numerous challenges, including limited visibility in underwater scenes, mutual occlusion and overlap among objects, and the dynamic similarity in appearance, color, and texture between the background and foreground. These factors significantly complicate the counting process. To address the scarcity of video-based indiscernible object counting datasets, we have developed a novel dataset comprising 50 videos, from which approximately 800 frames have been extracted and annotated with around 40,800 point-wise object labels. This dataset accurately represents real underwater environments where indiscernible marine objects are intricately integrated with their surroundings, thereby comprehensively illustrating the aforementioned challenges in object counting. To address these challenges, we propose a depth-assisted network with adaptive motion-differentiated feature encoding. The network consists of a backbone encoding module and three branches: a depth-assisting branch, a density estimation branch, and a motion weight generation branch. Depth-aware features extracted by the depth-assisting branch are enhanced via a depth-enhanced encoder to improve object representation. Meanwhile, weights from the motion weight generation branch refine multi-scale perception features in the adaptive flow estimation module. Experimental results demonstrate that our method not only achieves state-of-the-art performance on the proposed dataset but also yields competitive results on three additional video-based crowd counting datasets. The pre-trained model, code, and dataset are publicly available at <https://github.com/OUCVisionGroup/VIMOC-Net>.

Index Terms—Indiscernible marine objects, video object counting, depth-assisted visual perception, optical flow, motion-differentiated feature encoding.

I. INTRODUCTION

Large marine biological aggregations are crucial components of marine ecosystems, with fish schools serving as quintessential examples. These densely packed targets exhibit pronounced visual similarity and are visually indistinguishable, making them representative of indiscernible marine objects. Precisely quantifying their abundance and spatial distribution provides researchers with critical insights into their ecological functions and migratory behaviors. Accurate

The research has been supported by the National Natural Science Foundation of China under Grant 62371431 and 61906177, in part by the Marine Industry Key Technology Research and Industrialization Demonstration Project of Qingdao under Grant 23-1-3-hygg-20-hy, and in part by the Fundamental Research Funds for the Central Universities under Grants 202262004. (Corresponding author: Kunqian Li)

Chengzhi Ma, Kunqian Li, Shuaixin Liu, and Han Mei are with the College of Engineering, Ocean University of China, Qingdao 266404, China (machengzhi@stu.ouc.edu.cn; likunqian@ouc.edu.cn; liushuaixin@stu.ouc.edu.cn; meihan@stu.ouc.edu.cn).

enumeration of indiscernible marine objects is essential to develop more effective strategies for marine conservation and resource management [1].

However, in underwater environments, light refraction and scattering reduce the visual quality of imaging [2], presenting substantial challenges for the observation and enumeration of indiscernible marine objects. Marine objects often aggregate closely, resulting in occlusion and overlap, further complicating the counting process. Moreover, the apparent scale of marine objects is dynamically changed by both their variable swimming speeds and fluctuating distances from the camera, altering perceived size and morphology. Collectively, these factors significantly increase the complexity of accurately counting indiscernible marine objects.

Furthermore, underwater environments frequently feature complex backgrounds [3]. Background elements often exhibit similar appearance, color, and texture to the marine objects in the foreground, particularly under poor lighting conditions, leading to potential confusion between background and foreground objects. Consequently, distinguishing foreground objects becomes more challenging, thus complicating the accurate counting of indiscernible marine objects. Therefore, counting objects in underwater scenes necessitates not only addressing challenges associated with motion but also effectively differentiating foreground objects from the background.

Previous research on object counting has focused mainly on crowd counting [4]–[11], vehicle counting [12]–[15], and plant counting [16]–[18]. However, existing approaches face significant challenges when applied to the unique task of indiscernible object counting in marine environments. The IOCFormer [1] was developed to address these challenges by integrating density-based and regression-based strategies into a unified framework. Although it is designed to count indiscernible objects within single images in static scenarios, extending its application to video-based counting remains an open challenge. Compared to single-image object counting, video provides continuous spatio-temporal information, which enhances the potential for improving the robustness and accuracy of indiscernible object counting. However, existing video counting methods have predominantly focused on crowd counting tasks [19]–[25], but can hardly handle the distinct challenges associated with counting objects in complex and indiscernible underwater environments, including far more intricate backgrounds, indistinguishable individual appearance differences, and variable movement speeds across diverse scenes. Consequently, this paper addresses the task of counting

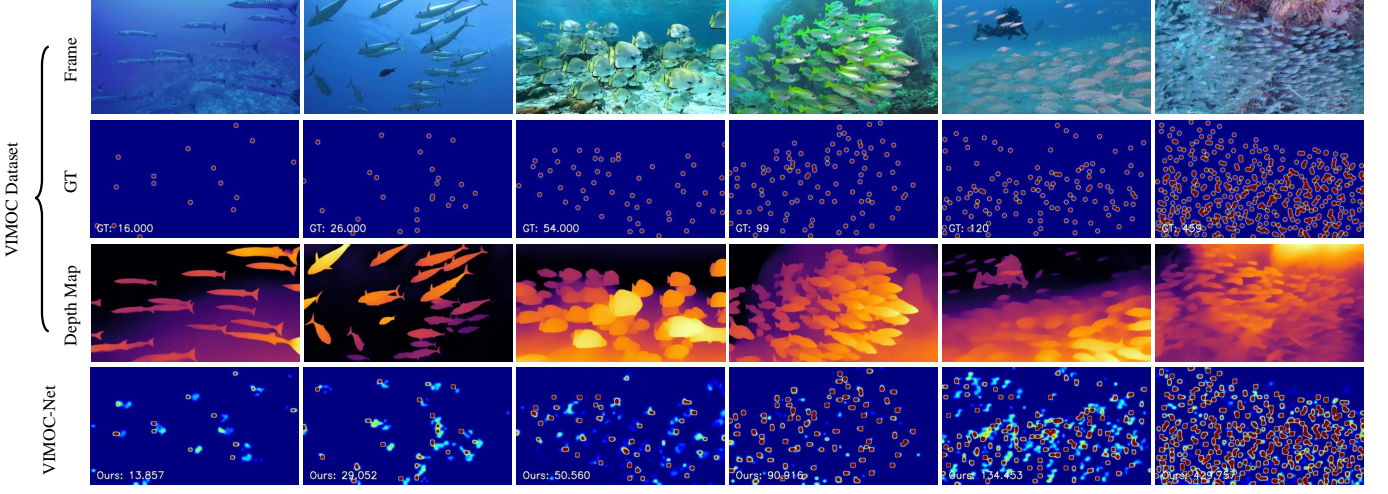


Fig. 1. Example of the proposed Video Indiscernible Marine Object Counting dataset (VIMOC dataset) and the prediction of our VIMOC-Net. From top to bottom: sampling frames, the corresponding pixel markers of indiscernible objects, the depth maps estimated with the Depth Anything [26], and our prediction.

objects in indiscernible underwater video scenes.

In this paper, to address the novel challenges and opportunities in video-based indiscernible object counting, we introduce a depth-assisted network with adaptive motion-differentiated feature encoding, termed VIMOC-Net, which aims to highlight the individual appearance difference of marine indiscernible objects and better describe them with motion cues. Beyond that, to further facilitate the study of this novel task, we have established a new video-based indiscernible marine object counting dataset (VIMOC Dataset). This dataset comprises 50 high-definition fish videos, with each 10th frame annotated, resulting in approximately 40,800 annotated points in total. In addition, we utilized the currently advanced depth estimation method - Depth Anything [26], to provide single-frame relative depth maps for the dataset, facilitating the research on object counting under a multi-task learning framework guided by depth estimation tasks. Illustrations of the newly established VIMOC dataset and predictions generated by the proposed VIMOC-Net are presented in Fig. 1. The primary contributions of this paper are as follows:

- A depth-assisted network with adaptive motion-differentiated feature encoding is proposed for indiscernible marine object video counting. To enhance the spatial feature representation of indiscernible objects, we design a depth-enhanced encoder that leverages depth-aware features to refine the regions containing such objects.
- An adaptive flow estimation module is designed that employs motion weights to perform adaptive flow estimation on multi-scale perception features, effectively addressing the issue of motion scale variations caused by differing indiscernible object movement speeds in underwater scenes.
- We establish a new video-based underwater indiscernible object counting dataset, containing 50 videos, 800 images, and 40,800 accurately annotated points. We compare our method with 11 mainstream counting models and the results show that our method outperforms all 11 models on this dataset.

II. RELATED WORKS

A. Image-based Object Counting

In the field of image-based object counting, current research predominantly focuses on crowd counting. Notable benchmarks in this domain include ShanghaiTech [4], UCF-QNRF [6], JHU-CROWD [9], and NWPU-Crowd [8]. The existing image-based object counting methods can be broadly categorized into three main approaches based on their counting strategies: detection, regression, and density map generation.

The detection-based object counting method [27]–[30], which identifies individual objects before counting, generally performs well in sparse scenes. However, accuracy can be significantly compromised in dense scenes due to occlusion and overlap among objects, leading to enumeration errors of individual entities. In contrast, regression-based counting methods [31], [32] directly predict the coordinates of target objects within an image and employ deep learning architectures to establish a mapping between image features and object counts. While this approach can partially alleviate the occlusion issue in dense scenes, its counting accuracy may remain insufficient when handling tightly packed objects, such as the indiscernible marine objects on which this paper focuses. The density map-based approach [4], [5], [10], [33] generates a density map to estimate the spatial distribution of objects and subsequently counts them by predicting the target density. For example, IOCFormer [1] integrates density-based and regression-based counting methodologies within a unified framework, leveraging the advantages of both approaches to enhance the accuracy of indiscernible object counting in underwater environments. Meanwhile, CrowdDiff [34] uses a diffusion model to generate high-fidelity density maps, although this approach requires a comparatively longer training period. In addition to the aforementioned approaches, another category of methods [35]–[38] improves the accuracy of the counting by using improved loss functions.

However, a single image provides only static information about the scene and objects of interest. Precisely localizing

densely aggregated and indiscernible objects, such as highly occluded and densely packed fish in marine environments, within this static context poses significant challenges.

B. Video-based Object Counting

Videos provide continuous spatio-temporal variation information, where spatial structure cues and motion dynamics within frames offer significant potential to improve the accuracy and robustness of counting algorithms. The core issues focused by existing methods include the acquisition of density maps and the methodologies for feature association and fusion under spatio-temporal constraints.

As an early attempt, ConvLSTM [19] uses a bidirectional convolutional LSTM to capture long range temporal information. LSTN [20] first uses a convolutional neural network to estimate the density map for each frame, and then uses a spatial transformer network (STN) [39] to model the relationship between the density maps of adjacent frames. MOPN [21] integrates an optical flow pyramid with an pre-trained feature extractor, incorporating motion information via multi-scale embeddings derived from optical flow for the joint prediction of density maps. EPF [22] proposes a flow-based method to estimate crowd density in video sequences, advocating that the flow of people across image locations should be estimated between successive frames, with the flow density inferred from these image streams instead of using direct regression. STGN [23] creatively estimates the density of the crowd in videos by modeling the relationship between pixels and patches within the local spatio-temporal domain through the introduction of a pyramid graph module. FRVCC [24] introduces a frame-recurrent mechanism that recursively correlates density maps across the temporal dimension, thereby effectively leveraging long-term interframe information and ensuring the temporal consistency of feature map responses. MAF [25] introduces moving foreground attention, which extracts motion features through two-way frame differencing and combines these motion features with the static features of the current frame to estimate the crowd count.

However, the existing works primarily address crowd counting in videos, the challenge of counting indiscernible objects in marine environments presents more formidable obstacles, including complex backgrounds, indistinguishable target appearances, and varying movement speeds across different scenes. In this paper, we utilize depth-aware features to enhance the differentiation of indiscernible objects. Furthermore, we propose adaptively encoding motion-differentiated features using flow guidance, thereby enhancing the learning of more reliable and reasonable features across varying motion rates.

C. Visual Object Counting with Auxiliary Data

In visual counting tasks, in addition to fully exploiting information from RGB images, a prevalent strategy is to integrate additional auxiliary data, such as depth maps and thermal, to provide additional cues. This has made RGB-Depth (RGB-D) and RGB-Thermal (RGB-T) object counting particularly active research areas. For example, Lian et al. [40] proposed the RDNet model, which estimates crowd head counts using

RGB-D information while simultaneously locating heads with bounding boxes. The depth-adaptive kernel was introduced for more robust density map regression. Liu et al. [41] proposed a cross-modal collaborative representation learning framework aimed at comprehensively capturing complementary information across different modalities, thus improving counting performance. TAFNet [42] is a novel three-stream network specifically designed for RGB-T crowd counting, which adaptively integrates RGB and thermal images, thus improving adaptability and achieving higher accuracy in complex environments. More recently, CSA-Net [43] introduced a scale-sensing cross-modal feature aggregation module and a scale-aware channel attention aggregation module to improve the performance of RGB-T crowd counting. Meng et al. [44] introduced a novel triple-modal learning framework for multi-modal crowd counting, which incorporates an auxiliary broker modality generated via a lightweight fusion model.

However, we observe that all of the aforementioned schemes require auxiliary data as input for model prediction, which is impractical in numerous scenarios and incurs additional application costs. In this paper, we concentrate on integrating auxiliary data as supplementary supervision during the model training phase, rather than employing them directly as part of the model input. This approach helps to better adapt it to video tasks and expand the application scenarios of the algorithm.

III. PROPOSED METHOD

Similar to the concept of terrestrial video crowd counting [23]–[25], which builds upon the task of image object counting, we define underwater video indiscernible object counting as the estimation of the number of indiscernible underwater objects in a single frame, utilizing information from consecutive frames within the video sequence. As a novel attempt for the above new challenging task, we introduce VIMOC-Net, a depth-assisted network that incorporates adaptive motion-differentiated feature encoding to address the challenges associated with indiscernible object counting in underwater videos. In this section, we first provide an architectural overview and analysis of VIMOC-Net, followed by a detailed description of its key modules.

A. Architectural Overview and Analysis of VIMOC-Net

The overall framework of VIMOC-Net is shown in Fig. 2. It comprises a backbone encoding module and three branches: the density estimation branch, the depth-assisting branch, and the motion weight generation branch. The depth-assisting and motion weight generation branches serve as auxiliary components that enhance the performance of the density estimation branch by providing spatio-temporal guidance, thereby improving the accuracy of predictions for indiscernible objects in complex underwater environments where static information alone is inadequate.

1) *Backbone Encoding Module*: We leverage the first 13 layers of VGG16 [45] and the Contextual Module from CAN [7] to construct the backbone encoding module. Both the preceding frame $I_{t-1} \in \mathbb{R}^{H \times W \times 3}$ and the current frame $I_t \in \mathbb{R}^{H \times W \times 3}$ are fed into the encoder, which extracts

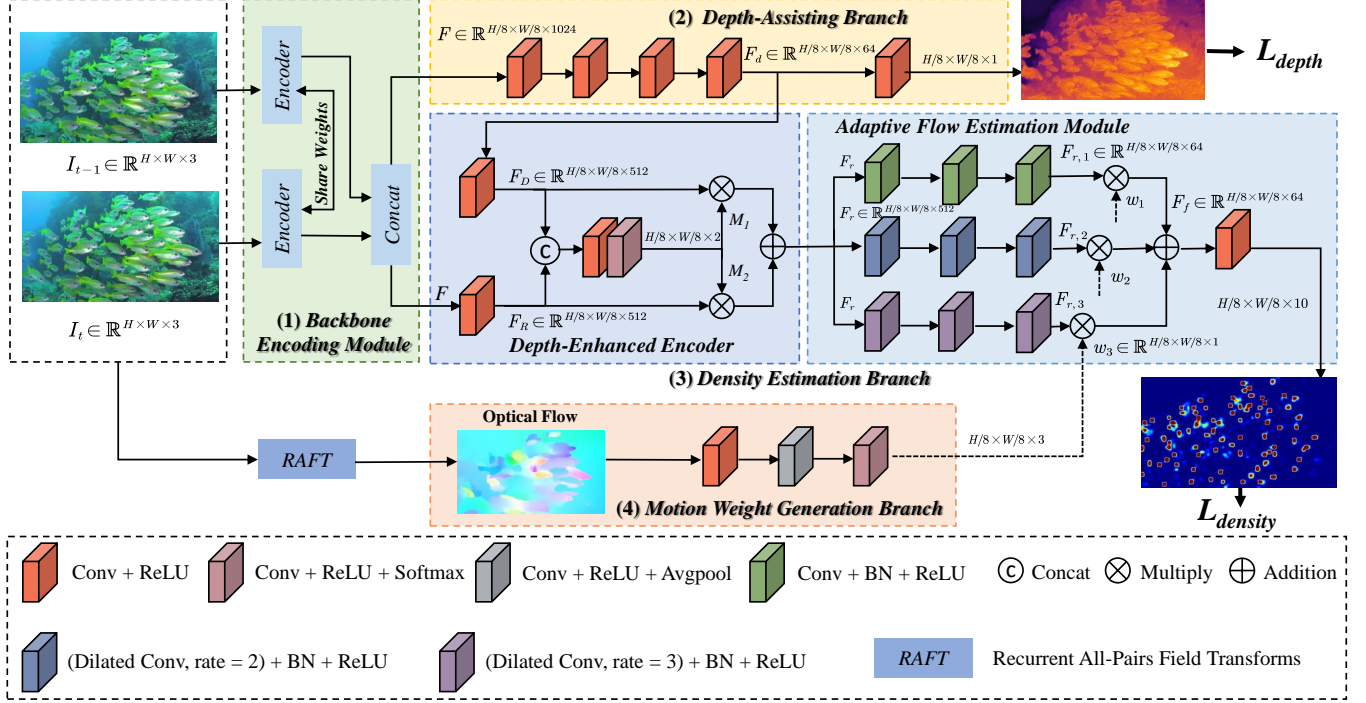


Fig. 2. The framework of the proposed VIMOC-Net, which is a depth-assisted indiscernible marine object counting network with adaptive motion-differentiated feature encoding. The network input consists of the previous frame I_{t-1} and current frame I_t . After feature extraction by a shared encoder, the features from both frames are concatenated into a feature map F , which is then fed into the depth-assisting branch and density estimation branch. The depth-enhanced encoder leverages depth-aware features F_d to improve indiscernible object features. The adaptive flow estimation module applies motion weights w_i to estimate flow adaptively on multi-scale perception features.

high-dimensional features from each frame, reducing the spatial dimensions to one-eighth of their original size. The extracted features from the two frames are then concatenated to form a fused feature map $F \in \mathbb{R}^{H/8 \times W/8 \times 1024}$, which is subsequently processed by both the depth-assisting branch and the depth-enhanced encoder (DEE) to facilitate advanced perception and transformation.

2) *Depth-Assisting Branch*: The depth-assisting branch is designed to leverage a joint-learning depth estimation sub-task to learn feature representations that incorporate image depth perception. These learned auxiliary features are subsequently integrated into the main branch, the density estimation branch, to improve its performance. The depth-assisting branch processes the feature map F through a depth decoder composed of four convolutional layers, each equipped with 3×3 kernels and ReLU activation functions. The resulting output features are denoted as $F_d \in \mathbb{R}^{H/8 \times W/8 \times 64}$. Thereafter, the branch head transforms F_d into a non-negative, single-channel depth map D , which is supervised by the pseudo ground truth depth map generated using Depth Anything [26]. The depth loss L_{depth} is calculated as the mean squared error (MSE) between the predicted depth map D and the corresponding ground truth depth reference. As derived from the intermediate layers of the depth-assisting branch, the feature map F_d can be regarded as a depth-aware representation that encapsulates rich spatial information to help distinguish indiscernible object instances.

In this depth-assisting branch, given the computational and fine-tuning costs associated with the main branch task, we opted not to directly adopt Depth Anything as the branch

architecture. Instead, we employed a knowledge distillation approach, retraining with the generated predictions from Depth Anything. This method provides an effective, low-cost solution aimed at obtaining enough robust representations of auxiliary features for the counting task.

3) *Density Estimation Branch*: The density estimation branch constitutes the central component of VIMOC-Net. This branch integrates auxiliary information from both the depth-assisting branch and the motion weight generation branch to achieve multi-scale spatio-temporal feature fusion, ultimately generating a density map and estimating the quantity of indiscernible marine objects.

Specifically, in the depth-enhanced encoder, designed to generate feature representations of counting targets with improved spatial perception capabilities, the feature map F from the backbone encoding module and the depth-aware feature map F_d from the depth-assisting branch are fused to obtain refined features $F_r \in \mathbb{R}^{H/8 \times W/8 \times 512}$. A more comprehensive description of the fusion procedure within the depth-enhanced encoder is provided in Section III-B.

To further enhance the feature representation's capability to characterize multiple motion scales for density estimation, we developed an adaptive flow estimation module. This module consists of three groups of parallel stacked dilated convolution layers on multiple scales with F_r as input, which allows more robust and versatile feature extraction. To further adaptively learn and predict the optimal weights for each group, we incorporate the output of the motion weight generation branch as the predicted weights. Subsequently, multi-scale perception

features extracted from various dilated convolution layers are adaptively fused. Ultimately, the density flow prediction is generated through the density head. Detailed information is provided in Section III-C.

4) *Motion Weight Generation Branch*: As mentioned earlier, while multi-scale perception features can be extracted via multi-parameter dilated convolutions, it is crucial to appropriately fuse these features in a differentiated manner by incorporating the motion scale information from the current frame. Given the significance of optical flow as a critical motion perception technique for video analysis, we have developed a mechanism that leverages optical flow transformation to automatically predict weights for multi-scale perception features. The optical flow between the preceding frame I_{t-1} and the current frame I_t is calculated utilizing the RAFT model [46]. The resultant optical flow is subsequently fed into the Motion Weight Generation (MWG) branch to obtain the motion weights $w_i \in \mathbb{R}^{H/8 \times W/8 \times 1}$, where $i = 1, 2, 3$. This process is detailed in Section III-C.

B. Depth-Enhanced Encoder for Spatial Information Fusion

The depth-enhanced encoder (DEE) leverages depth-aware features F_d to integrate with the encoder's feature mapping F , thereby enhancing the spatial identifiability of indiscernible objects and improving the robustness of feature representation in complex underwater environments.

Fig. 3 delineates the intricate architecture of the depth-enhanced encoder. Initially, DEE employs two parallel convolutional blocks to project the depth-aware features F_d and the backbone encoding feature map F into a 512-channel space, ensuring channel alignment for subsequent addition fusion. To enhance the integration of spatial perception from F_d and appearance perception from F , we introduce an element-wise fusion weight learning strategy. Specifically, the aligned depth features $F_D \in \mathbb{R}^{H/8 \times W/8 \times 512}$ are concatenated with the transformed backbone encoding features $F_R \in \mathbb{R}^{H/8 \times W/8 \times 512}$. This concatenated feature set is then processed through two Conv-ReLU layers to learn joint feature representations. Subsequently, these learned features pass through the Softmax activation function to generate normalized element-wise fusion weights $M_1 \in \mathbb{R}^{H/8 \times W/8 \times 1}$ and $M_2 \in \mathbb{R}^{H/8 \times W/8 \times 1}$, which are applied for F_R and F_D , respectively. This process ultimately yields the refined features $F_r \in \mathbb{R}^{H/8 \times W/8 \times 512}$ as follows

$$F_r = M_1(F_R, F_D) \otimes F_R + M_2(F_R, F_D) \otimes F_D, \quad (1)$$

where \otimes denotes element-wise multiplication.

We can notice that, by effectively capturing depth information, the model can more accurately differentiate between foreground and background elements. Moreover, these features help identify and improve visually ambiguous target objects, leading to more detailed and precise feature representation. This capability strengthens the predictive performance of the density estimation branch, enabling a more accurate estimation of object density distributions, especially in scenes with complex backgrounds and similar textures. Consequently, the model not only helps achieve superior performance in

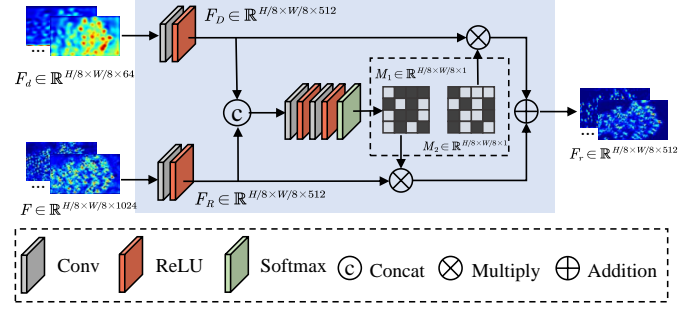


Fig. 3. Detailed structure of the Depth-Enhanced Encoder (DEE).

counting tasks, but also provides a robust solution for detecting indiscernible objects in complex underwater scenes.

C. Motion Temporal Perception for Adaptive Flow Estimation

Unlike terrestrial crowd counting tasks, where the movement speed of individuals under a fixed perspective is relatively constant, the velocity of underwater indiscernible objects (such as schools of fish) exhibits significant variability. Furthermore, the continuous motion of the underwater camera during recording introduces additional complexity, resulting in diverse and unpredictable motion scales of the objects that are counted in the video footage. To better perceive the diverse temporal motions of indiscernible objects, an optical flow-based method is employed to dynamically track motion information and highlight changes in movement characteristics. Then, to address the challenge of varying motion scales in underwater object counting, a multi-stream architecture is utilized to capture features at different motion scales. Furthermore, motion weight-based adaptive fusion is applied to emphasize the most relevant features of moving objects.

Fig. 4 presents the detailed architecture of the adaptive flow estimation module and the motion weight generation process. The adaptive flow estimation module comprises two essential components: the motion enhancement module (MEM), which captures features across various motion scales, and the adaptive flow feature fusion mechanism (AFFF), which mitigates environmental interference by accentuating significant features. With F_r as input, the MEM adopts a multi-stream architecture to extract features across various motion scales. Each stream is specifically designed to capture features from different receptive fields by using convolutions with varying dilation rates. More precisely, each stream consists of three convolutional layers, each incorporating a convolution kernel, batch normalization, and a ReLU activation function. The convolution kernels in each stream are distinct: the first stream utilizes standard 3×3 convolutions, the second employs dilated 3×3 convolutions with a dilation rate of 2, and the third applies dilated 3×3 convolutions with a dilation rate of 3. Using dilated convolutions, the receptive field of each layer is significantly enlarged without an increase in the number of parameters. This architectural design allows the model to effectively capture multi-scale perception features while preserving computational efficiency. The specific receptive

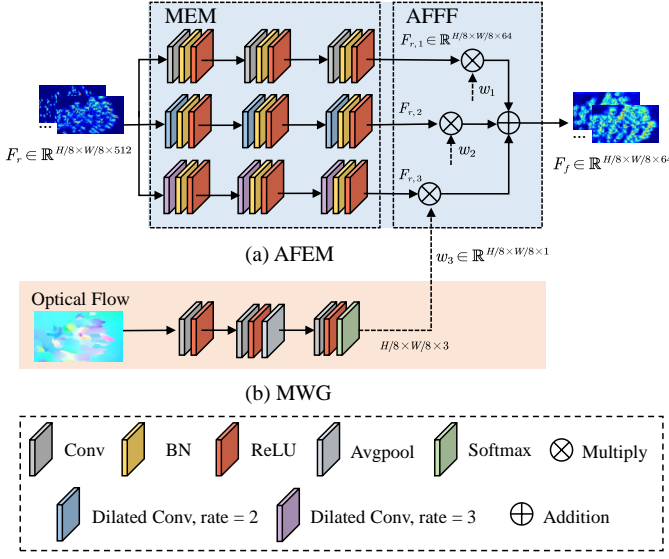


Fig. 4. Detailed structures of the Adaptive Flow Estimation Module (AFEM) and the Motion Weight Generation (MWG). The AFEM is composed of the motion enhancement module and the adaptive flow feature fusion.

fields of the motion enhancement module are detailed in Table I.

The features extracted at various motion scales by the MEM are denoted as $F_{r,i} \in \mathbb{R}^{H/8 \times W/8 \times 64}$, for $i = 1, 2, 3$. Subsequently, these features are adaptively fused using the motion weights w_i . The process of adaptive flow feature fusion is defined as follows:

$$F_f = \sum_{i=1,2,3} w_i \otimes F_{r,i}, \quad (2)$$

$$w_i = \frac{e^{w_i}}{\sum_{i=1,2,3} e^{w_i}}, i = 1, 2, 3, \quad (3)$$

where w_i , for $i = 1, 2, 3$, represents the fusion weights generated by the motion weight generation branch.

Instead of using fixed weight ratios for motion features $F_{r,i}$ during fusion at each scale, we employ adaptive motion weights, which allows the model to dynamically adjust to complex underwater environments with varying target motion speeds. Moreover, by more effectively aligning with the actual data distribution, adaptive fusion not only mitigates overfitting but also enhances model flexibility between training and test sets, thereby improving generalization to new application scenarios. In Section IV-C2, we perform ablation studies to verify the superiority of motion weight-guided fusion over fixed weight fusion.

D. Object Flow Conservation Constraint

With the fused feature $F_f \in \mathbb{R}^{H/8 \times W/8 \times 64}$, the density head predicts the density flow for indiscernible marine object counting. Specifically, we integrate the conservation constraint from EPF [22] to estimate the density in the current frame I_t by applying a flow prediction strategy between the preceding frame I_{t-1} and the current frame I_t . The conservation constraint stipulates that the density at a given position at time t

TABLE I
THE RECEPTIVE FIELD OF THE DILATION CONVOLUTION LAYER.

Stream	Top			Middle			Bottom		
Layer	1	2	3	1	2	3	1	2	3
Dilation rate	1				2				3
Receptive field ($n \times n$)	3	5	7	5	9	13	7	13	19

can only originate from adjacent grid positions at time $t - 1$ and flow to adjacent grid positions at time $t + 1$, including the position itself. This ensures that the model accounts for objects that remain stationary in the same position. Our model outputs a downsampled density map, where each grid position corresponds to an 8×8 pixel block in the input image. This downsampling rate is commonly used in crowd-counting models [5] [7] [22], as it strikes a good balance between the resolution of the density map and the computational efficiency of the model.

We denote the predicted flow direction between all adjacent locations from time $t - 1$ to time t using $f^{t-1,t}$. In practice, $f^{t-1,t}$ shares the same dimensions as the image grid, with 10 channels assigned per location. The first nine channels correspond to the eight neighboring positions that surround a given grid point, along with the position itself. The tenth channel signifies potential flow originating from outside the image boundaries, which holds significance only at the grid's edges. Let m_j^t represent the number of fish in the grid position j at time t , and let $f_{i,j}^{t-1,t}$ denote the number of fish that transitioned from grid position i to the grid position j between times $t - 1$ and t . For all non-edge positions j , the conservation constraint can be formulated as:

$$m_j^t = \sum_{i \in N(j)} f_{i,j}^{t-1,t}, \quad (4)$$

where $N(j)$ represents the 8 neighbours surrounding grid location j , including j itself, to account for fish that remain in the same location. Let m_j^t be the aggregate flow of fish in the grid position j at time t , then the predicted total count for the entire image can be obtained by summing all m_j^t values. If the direction of the video sequence is reversed, the flow vector should exhibit the same magnitude but an opposite direction. This relationship can be expressed as:

$$f_{i,j}^{t-1,t} = f_{j,i}^{t,t-1}. \quad (5)$$

E. Loss Function

In line with previous research [4], [5], [7], [22], we employ a similar methodology to generate the ground truth of the density map. Specifically, each image is annotated with n two-dimensional points $\{P_i^t\}_{i=1}^n$, which indicate the positions of the counting targets within the scene. The corresponding true density map \hat{m}_j^t is generated through the convolution of binary images, where pixels at specified positions are set to 1 and all other pixels are set to 0, with a Gaussian kernel $N(\cdot | \mu, \sigma^2)$ characterized by a mean of μ and a standard deviation of σ .

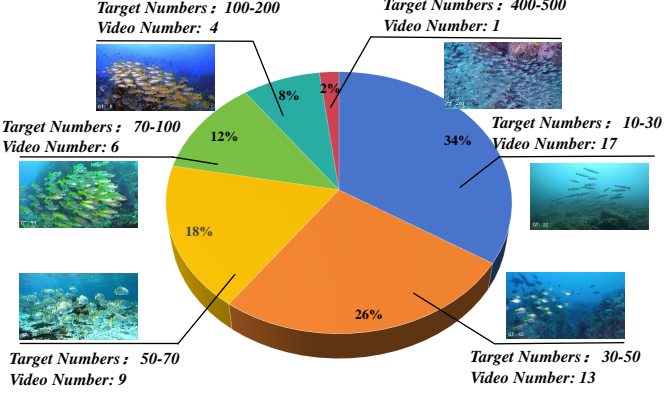


Fig. 5. The proportion of indiscernible objects within specific number ranges across the entire video dataset. A representative sample from each number range is selected for display, with the corresponding count labeled at the lower left corner of each sample.

The true density value for any position j within the image can be written:

$$\hat{m}_j^t = \sum_{i=1}^n N(p_j \mid \mu = P_i^t, \sigma^2), \quad (6)$$

where p_j denotes the center of location j , and σ is set to 3 following standard recommendations.

We input the previous frame I_{t-1} and the current frame I_t into the network for training to obtain the fish flow estimate. The predicted density m_j^t of I_t is derived from conservation constraints as given in Eq. (4). To ensure that the predicted density aligns with the actual density, we employ a flow loss function L_{flow} to quantify the discrepancy between the predicted and actual density values, which is expressed as:

$$L_{flow} = \sum_{j \in I_t} (\hat{m}_j^t - m_j^t)^2, \quad (7)$$

where \hat{m}_j^t denotes the actual density value at time t and position j , while m_j^t represents the predicted density value at the same time and position. Then, we enforce the constraint in Eq. (5) by employing the cycle consistency loss L_{cycle} , formulated as follows:

$$L_{cycle} = \sum_{j \in I_t} \sum_{i \in N(j)} \left(f_{i,j}^{t-1,t} - f_{j,i}^{t,t-1} \right)^2. \quad (8)$$

The density loss $L_{density}$ is computed by summing L_{flow} and L_{cycle} . Along with the depth loss L_{depth} of the depth-assisting branch introduced in Section III-A2, which utilizes mean square error (MSE) loss, the total loss function for VIMOC-Net is formulated as:

$$L = L_{flow} + L_{cycle} + L_{depth}. \quad (9)$$

IV. EXPERIMENT

A. Implementation Details and Experimental Setting

1) *Implementation Details*: During the training process, the Adam optimizer [47] was employed for optimization. The initial learning rate was set to 1×10^{-4} , with a weight decay of 5×10^{-4} . A batch size of 1 and input image dimensions

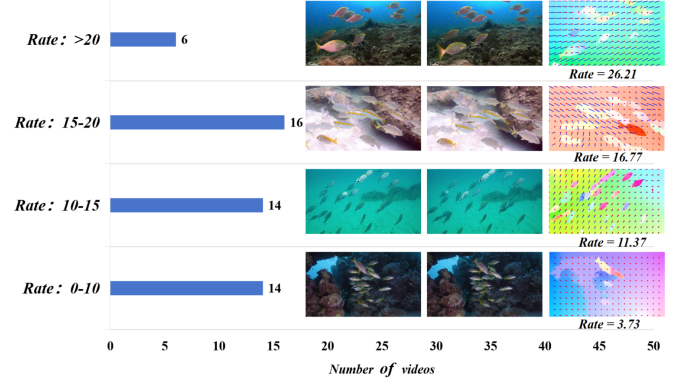


Fig. 6. The proportion of the motion rate range for indiscernible objects is presented. A representative sample from each rate range is selected and its motion rate is displayed.

of 640×360 were utilized. All experiments were conducted on a consistent hardware configuration consisting of a single NVIDIA RTX 3090 GPU, a 2.3 GHz Intel Xeon processor, 64 GB RAM, and the Ubuntu 18.04 operating system.

2) *Dataset*: We have established an indiscernible marine object counting dataset comprising 50 fish video sequences. The frames were extracted at intervals of every 10 frames, yielding a total of 800 images annotated with approximately 40,800 precise points. This dataset encompasses a diverse array of fish species and schooling configurations, ranging from small clusters to densely packed formations, thereby demonstrating a high degree of diversity and complexity. In Fig. 5, we present the distribution of fish densities along with illustrative examples. Of the total videos, 60% (30 out of 50) contain $0 \sim 50$ fish. Additionally, 30% (15 out of 50) of the videos contain $50 \sim 100$ fish. Notably, 5 videos (10%) feature more than 100 fish, with an exceptional case containing $400 \sim 500$ fish. This density distribution of the counting targets offers a basis for evaluating the performance of the indiscernible object counting method across varying densities.

Furthermore, we employ optical flow to analyze and categorize the movement velocity of the counting targets. Optical flow comprises horizontal and vertical components, from which we derive the motion rate by integrating these components, which can be expressed as:

$$Rate = \frac{1}{n} \sum_{i=1}^n \sqrt{(u_i)^2 + (v_i)^2} \quad (10)$$

where n denotes the number of pixels, u_i and v_i represent the horizontal and vertical components of optical flow on pixel i , respectively. In Fig. 6, the videos are categorized according to their corresponding motion rates. Specifically, scenes exhibiting a motion rate below 15 are classified as slow-motion scenes, whereas those with a motion rate exceeding 15 are designated as fast-motion scenes. Within our dataset, there are 28 videos of slow-motion scenes and 22 videos of fast-motion scenes. This classification framework provides robust support for evaluating the model's performance in indiscernible object counting across varying motion rates.

To ensure the scientific rigor and effectiveness of model training and evaluation, we designed a series of three cross-

TABLE II

QUANTITATIVE RESULTS COMPARING OUR PROPOSED METHOD AGAINST STATE-OF-THE-ART TECHNIQUES ON THE NEWLY INTRODUCED VIDEO DATASET. THE BEST PERFORMING RESULTS ARE HIGHLIGHTED IN BOLD. “TEST” REFERS TO THE ENTIRE TEST SET, “SLOW” DENOTES THE SUBSET WITH SLOW-MOTION RATE, AND “FAST” REPRESENTS THE SUBSET WITH FAST-MOTION RATE. THE FINAL INDEX IS DERIVED BY AVERAGING THE RESULTS OF THREE CROSS-VALIDATION EXPERIMENTS, WITH THE “ \pm ” SYMBOL INDICATING THE STANDARD DEVIATION OF THE ERRORS.

Method	Input	Type	Test		Slow		Fast	
			MAE \downarrow	RMSE \downarrow	MAE \downarrow	RMSE \downarrow	MAE \downarrow	RMSE \downarrow
CSRNet [5]	Image	RGB	12.88 \pm 3.1	17.49 \pm 4.2	13.13 \pm 3.4	17.57 \pm 4.5	11.06 \pm 4.4	15.70 \pm 6.9
CAN [7]	Image	RGB	11.36 \pm 2.1	15.64 \pm 2.4	11.08 \pm 3.7	14.61 \pm 4.6	11.72 \pm 4.5	15.03 \pm 5.2
BL [35]	Image	RGB	11.28 \pm 1.9	15.85 \pm 2.3	10.46 \pm 3.3	14.22 \pm 4.2	12.02 \pm 3.9	15.88 \pm 4.5
DMCount [36]	Image	RGB	10.67 \pm 1.7	15.01 \pm 2.8	10.81 \pm 2.9	14.24 \pm 3.8	11.51 \pm 2.6	15.32 \pm 3.5
P2PNet [31]	Image	RGB	10.21 \pm 1.9	14.64 \pm 2.9	11.11 \pm 2.4	15.45 \pm 3.4	9.36 \pm 2.1	13.56 \pm 2.9
CMCRL [41]	Image	RGB-D	10.25 \pm 1.5	14.47 \pm 2.8	10.45 \pm 1.7	14.89 \pm 3.3	10.02 \pm 2.0	14.14 \pm 3.4
GL [37]	Image	RGB	9.65 \pm 0.8	13.58 \pm 1.4	9.16 \pm 1.6	12.13 \pm 2.1	10.33 \pm 1.3	13.83 \pm 2.9
EPF [22]	Video	RGB	9.17 \pm 0.3	13.10 \pm 1.7	9.85 \pm 1.5	12.93 \pm 2.8	8.42 \pm 1.7	12.23 \pm 3.8
DEFNet [48]	Image	RGB-D	10.47 \pm 1.4	14.69 \pm 2.6	10.24 \pm 2.9	14.44 \pm 3.6	10.72 \pm 2.5	14.93 \pm 3.5
STGN [23]	Video	RGB	9.35 \pm 0.6	13.25 \pm 1.8	9.22 \pm 1.5	12.24 \pm 2.1	9.55 \pm 1.1	13.85 \pm 2.4
MAF [25]	Video	RGB	8.76 \pm 0.7	12.43 \pm 1.2	8.92 \pm 1.8	12.85 \pm 2.6	8.55 \pm 1.5	12.05 \pm 2.9
Ours	Video	RGB	7.80 \pm 0.8	11.21 \pm 0.9	8.19 \pm 2.3	11.82 \pm 3.1	7.23 \pm 1.7	10.67 \pm 3.1

validation experiments. In each experiment, the 50 video sequences were randomly partitioned into a training set and a test set, with 35 videos allocated for training and the remaining 15 reserved for testing. Importantly, each experiment utilized a distinct set of 15 non-overlapping videos as the test set. This splitting strategy not only provides comprehensive support for assessing the model’s performance under varying densities and motion speeds but also minimizes biases introduced by differences in data partitioning, thereby enhancing the stability and reliability of the experimental results. Furthermore, substantial variations in fish numbers and dynamic characteristics within the dataset facilitate the evaluation of the model’s capability to handle complex scenes, address occlusion challenges, and achieve accurate counting.

3) *Evaluation metrics*: To assess the counting performance of the proposed method, we employ mean absolute error (MAE) and root mean square error (RMSE) as evaluation metrics, i.e.,

$$MAE = \frac{1}{n} \sum_{i=1}^n |y_i - \hat{y}_i|, \quad (11)$$

$$RMSE = \sqrt{\frac{1}{n} \sum_{i=1}^n (y_i - \hat{y}_i)^2}, \quad (12)$$

where n denotes the number of test sample frames, y_i represents the true value, and \hat{y}_i indicates the predicted value.

B. Experimental Results and Analysis

We compared our proposed method against eleven mainstream counting models in the experiments. The compared methods include CSRNet [5], CAN [7], BL [35], DM-Count [36], P2PNet [31], CMCRL [41], GL [37], EPF [22], DEFNet

[48], STGN [23], MAF [25]. The methods we evaluate encompass both image-based and video-based counting techniques. Specifically, the video-based approaches include EPF [22], STGN [23] and MAF [25]. In addition, we compare methods that use auxiliary data to assist with counting, namely CMCRL [41] and DEFNet [48]. Both CMCRL [41] and DEFNet [48] utilize not only RGB images but also depth maps generated by Depth Anything as shared inputs.

The quantitative experimental results are presented in Table II. In addition to comprehensive evaluations on all videos within the test set, the test set has also been categorized according to motion rates to facilitate more detailed categorical assessments. In the table, “Test” denotes the entire test set, “Slow” indicates the test set with a slow-motion rate, and “Fast” corresponds to the test set with a fast-motion rate.

The results indicate that the proposed method consistently demonstrates superior performance across all test scenarios, markedly outperforming other prevalent methods. On the entire test set, our approach achieves a MAE of 7.80 and a RMSE of 11.21, highlighting its stable and exceptional performance. On the Slow test set, the MAE is 8.19, and the RMSE is 11.82, while on the Fast test set, the MAE and RMSE are 7.23 and 10.67, respectively. These results clearly indicate that our method outperforms all comparative methods in both the Slow and Fast test sets, achieving the best overall performance. This further validates its adaptability to different scene complexities and its robust counting capabilities.

Furthermore, to provide a more intuitive understanding of our method’s effectiveness across various scenes, we chose three most competitive comparison methods, i.e., EPF [22], STGN [23], and MAF [25], along with our proposed model for visual comparison. All of these methods are originally video counting models. The visualized results are presented in Fig. 7.

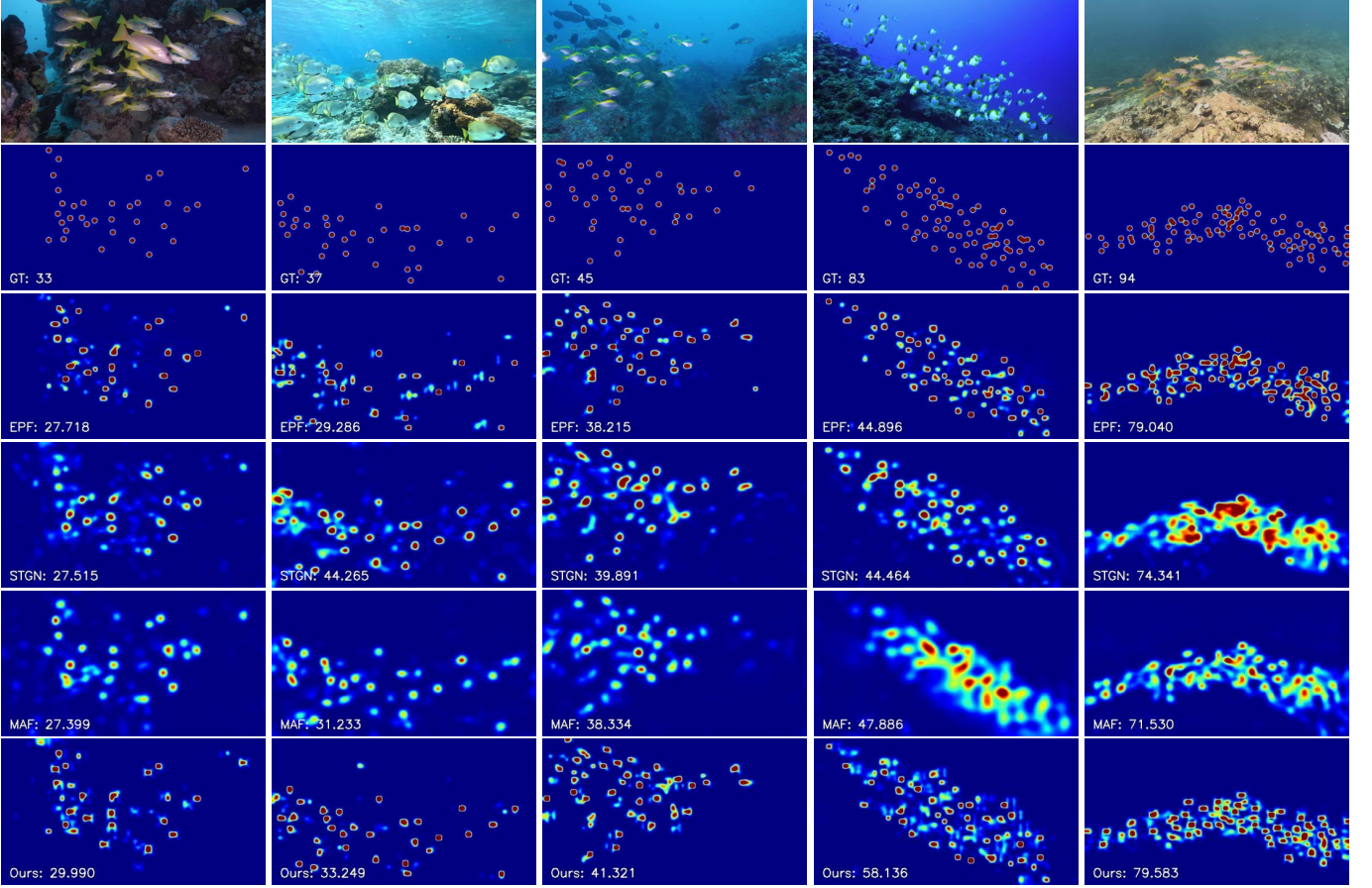


Fig. 7. Visualization of the counting results for EPF [22], STGN [23], MAF [25] and our proposed model. The ground truth (GT) or estimated counts for each scenario are displayed in the lower left corner of the respective images. The first two rows shows the input images along with their corresponding actual density maps, while the third to sixth rows illustrate the predicted density maps generated by the aforementioned models and our proposed model, respectively.

These visualizations effectively illustrate the advantages of our approach in various video contexts, providing robust support for a comprehensive analysis of model performance.

Our method outperforms other compared mainstream methods primarily due to the following two key innovations:

- Incorporation of Depth Perception: Our approach pioneers the integration of depth perception into the task of counting indiscernible objects in underwater environments. By leveraging a joint learning mechanism for depth perception, our method not only eliminates the necessity of directly incorporating depth as input, but also enhances the spatial representation and complexity modeling of underwater scenes. This enables the model to achieve robust and accurate performance in scenarios characterized by severe occlusion, challenging lighting conditions, and diverse shapes of objects.

- Multi-Scale Perception and Adaptive Fusion: We employ a multi-stream dilated convolutional architecture to capture features across various scales. Additionally, we integrate a motion-weighting mechanism that incorporates optical flow information into the network, adaptively emphasizing scale-differentiated features. This approach effectively mitigates the challenges posed by motion scale variations due to differing speeds, thereby ensuring high counting accuracy even in complex underwater environments.

TABLE III
THE RESULTS OF THE ABLATION STUDY ON THE DEPTH-ENHANCED ENCODER (DEE), MOTION ENHANCEMENT MODULE (MEM) AND ADAPTIVE FLOW FEATURE FUSION (AFFF), RESPECTIVELY. ALL EXPERIMENTS WERE CARRIED OUT ON THE PROPOSED DATASET.

DEE	MEM	AFFF	MAE \downarrow	RMSE \downarrow
✓	✓	✓	9.17 \pm 0.3	13.10 \pm 1.7
			8.62 \pm 0.5	12.65 \pm 1.1
			8.09 \pm 0.7	11.58 \pm 0.9
✓	✓	✓	7.80 \pm 0.8	11.21 \pm 0.9

C. Ablation Study

1) *Ablation Study on Key Modules:* To demonstrate the effectiveness of the core components in our network, we conducted a series of ablation studies designed to systematically evaluate the contributions of the depth-enhanced encoder and the adaptive flow estimation module. By progressively removing or modifying these components, we were able to assess their individual impact on overall performance. The experimental results, summarized in Table III, clearly illustrate the performance of the model in different configurations.

As illustrated in Table III, the incorporation of depth infor-

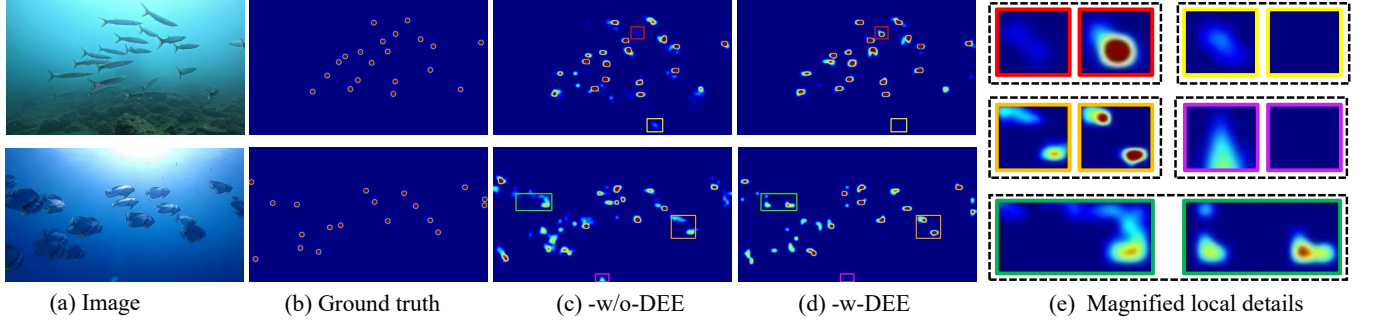


Fig. 8. Visualized results of the ablation study on the Depth-Enhanced Encoder (DEE). (c) and (d) show the results without and with the DEE, respectively. (e) provides a detailed comparison of five local regions, which more clearly demonstrates the improvement brought by the DEE. The yellow and pink boxes highlight that foreground objects are incorrectly detected in the background without the DEE, while the DEE significantly reduces these false detections. The other three boxes reveal that the model fails to correctly predict foreground objects without the DEE, but successfully predicts them with the DEE.

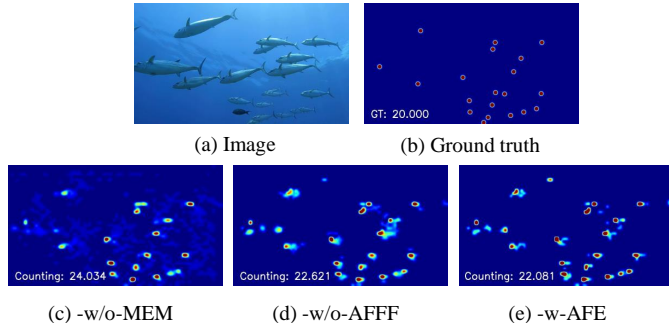


Fig. 9. Visualized comparison of the ablation study on MEM, AFFF and AFE modules. (c) -w/o-MEM: without motion enhancement module; (d) -w/o-AFFF: without adaptive flow feature fusion; (e) -w-AFE: with adaptive flow estimation, which integrates both motion enhanced module and adaptive flow feature fusion.

mation via the depth-enhanced encoder leads to a substantial improvement in density estimation, with reductions of 6.0% in MAE and 3.4% in RMSE. Fig. 8 shows the effectiveness of depth-aware features (depth-enhanced encoder) in improving density estimation. We compared the performance of the baseline model against that of the model incorporating the depth-enhanced encoder. The baseline model exhibited a significant number of false detections, including failures to predict foreground objects and erroneous classifications of background elements as foreground. By integrating depth features, the depth-enhanced encoder mitigates these errors, thereby improving the model’s ability to distinguish between foreground and background elements and enhancing foreground feature extraction. This improvement is particularly evident in the boxed regions highlighted in Fig. 8.

Furthermore, the method that incorporates adaptive flow estimation also showed significant improvements, reducing MAE and RMSE by 11.8% and 11.6%, respectively. Fig. 9 illustrates the significant benefits of the adaptive flow estimation module. The motion enhancement module is capable of effectively capturing the motion features of indiscernible objects, thereby ensuring accurate tracking and counting of object movements in complex scenes, particularly under conditions of significant background interference. In addition, the motion weight-guided adaptive fusion further improves the performance of

TABLE IV
EXPERIMENTAL COMPARISON BETWEEN SINGLE-STREAM AND MULTI-STREAM CONVOLUTIONAL LAYER STRUCTURES. THE SINGLE-STREAM CONVOLUTIONAL LAYER STRUCTURE COMPRISSES THREE DISTINCT CONFIGURATIONS OF CONVOLUTION LAYERS. THE MULTI-STREAM CONVOLUTIONAL LAYER STRUCTURE IS FURTHER CATEGORIZED INTO FIXED-WEIGHT FUSION AND ADAPTIVE MOTION WEIGHT-GUIDED FUSION.

MEM		MAE \downarrow	RMSE \downarrow
\times	3 \times 3 Conv, rate = 1	9.48 \pm 0.3	13.92 \pm 1.2
\times	3 \times 3 Conv, rate = 2	9.21 \pm 0.4	13.17 \pm 1.0
\times	3 \times 3 Conv, rate = 3	9.76 \pm 0.6	14.08 \pm 1.5
\checkmark	Fixed weights	8.34 \pm 0.8	12.61 \pm 1.1
\checkmark	Adaptive weights	8.09 \pm 0.7	11.58 \pm 0.9

the model. Through adaptive adjustment of these weights, the module can more flexibly and accurately capture multi-scale perception features.

2) *Ablation Study on Motion Weight-Guided Fusion*: We further conduct an ablation experiment to evaluate the effectiveness of using adaptive motion weight-guided fusion compared to fixed-weight fusion. In this experiment, we compare the performance of a single-stream dilated convolutional structure with that of a multi-stream dilated convolutional architecture. The multi-stream dilated convolutional architecture is further divided into two settings: fixed-weight fusion and adaptive motion weight-guided fusion. The experimental results are summarized in Table IV. This comparative analysis systematically evaluates the impact of different structures and fusion methods on model performance, validating the benefits of adaptive motion weights.

The fixed fusion weights are uniformly assigned as 1/3 for each component. Here, “3 \times 3 Conv, rate = 1” denotes a single-stream dilated convolutional structure utilizing a 3 \times 3 convolution kernel. Meanwhile, “3 \times 3 Conv, rate = 2” and “3 \times 3 Conv, rate = 3” indicate single-stream dilated convolutional structures that employ 3 \times 3 dilated convolution kernels with dilation rates of 2 and 3, respectively. We evaluated the performance of various convolutional architectures within the model. The results indicate that the adaptive fusion method employing

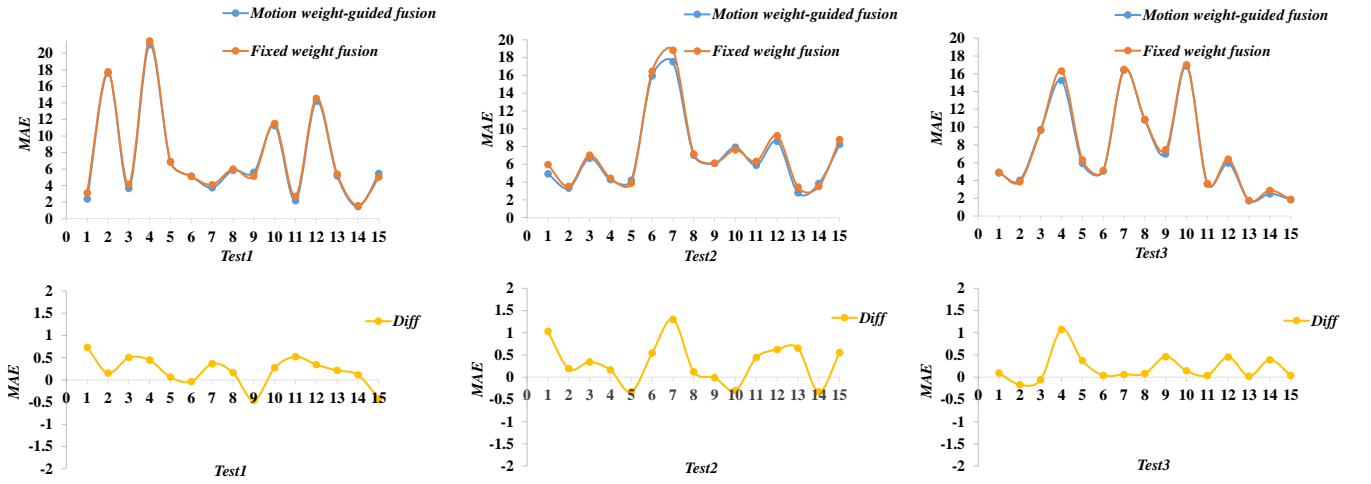


Fig. 10. Comparison of performance metrics (in terms of MAE) and analysis of differences between motion weight-guided fusion and fixed weight fusion. The first row illustrates the MAE comparison between the two fusion methods, whereas the second row highlights the performance discrepancies.

TABLE V

QUANTITATIVE COMPARISONS OF OUR RESULTS WITH STATE-OF-THE-ART METHODS ON THREE CROWD VIDEO DATASETS ARE PRESENTED. THE TOP AND SECOND-BEST PERFORMING RESULTS ARE HIGHLIGHTED IN **RED** AND **BLUE** FONTS, RESPECTIVELY.

Datasets		Classroom		Mall		FDST	
Method	Type	MAE \downarrow	RMSE \downarrow	MAE \downarrow	RMSE \downarrow	MAE \downarrow	RMSE \downarrow
CSRNet [5]	Image	3.42	3.86	1.84	2.34	1.98	2.51
BL [35]	Image	2.86	3.14	1.96	2.49	-	-
DMCount [36]	Image	2.86	3.94	2.02	2.52	-	-
LSTN [20]	Video	3.02	3.90	2.03	2.60	3.35	4.45
EPF [22]	Video	1.68	2.06	2.06	2.61	2.10	2.46
MAF [25]	Video	1.64	2.00	1.51	1.93	1.19	1.56
Ours	Video	1.54	1.83	1.75	2.22	1.81	2.35

motion-guided weights outperforms alternative approaches, validating its superiority. This method captures dynamic information more accurately through the use of motion-guided weights and substantially enhances the model's robustness in handling complex backgrounds and variations in target motion scales.

To more clearly demonstrate the superiority of using motion weights for adaptive fusion over fixed weight settings, we compare the MAE metrics for each test video in the three test sets, as shown in Fig. 10. The first row of the figure presents the MAE comparison between the two fusion methods, while the second row shows the differences. A positive difference indicates that the method using motion weight-guided fusion outperforms fixed weight fusion, whereas a negative difference suggests inferior performance. This allows for a more detailed observation of the impact of each fusion method on individual test videos.

D. Crowd Experimental Results and Analysis

To verify the generality of our model, we conduct experiments on three different crowd video datasets: Classroom [25], Mall [49], and FDST [20].

The Classroom dataset [25] was developed by recording videos in a classroom environment. The videos were captured with a frame interval of 10 frames, resulting in a total of 1,290 frames at a resolution of 1280×720 pixels. The number of individuals present in each frame varies considerably, ranging from a minimum of 1 to a maximum of 51, with an average of approximately 30.3 individuals per frame. Keeping with the methodology described in [25], the dataset has been divided into two equal parts, where the first half is designated for training purposes and the second half for testing.

The Mall dataset [49] was collected in a shopping mall equipped with surveillance cameras. This dataset captures both moving and stationary pedestrians under complex lighting conditions. It comprises 2,000 annotated video frames, each with a resolution of 640×480 pixels and a frame rate of less than 2 FPS. In accordance with the experimental setup described by Chen et al. [49], the first 800 frames are designated for training purposes, while frames 801 to 2,000 are reserved for testing.

The FDST dataset [20] is presently recognized as the largest and most comprehensive crowd video dataset, encompassing 100 videos across 13 diverse scenes in both indoor and outdoor settings. Each video consists of 150 frames and is available

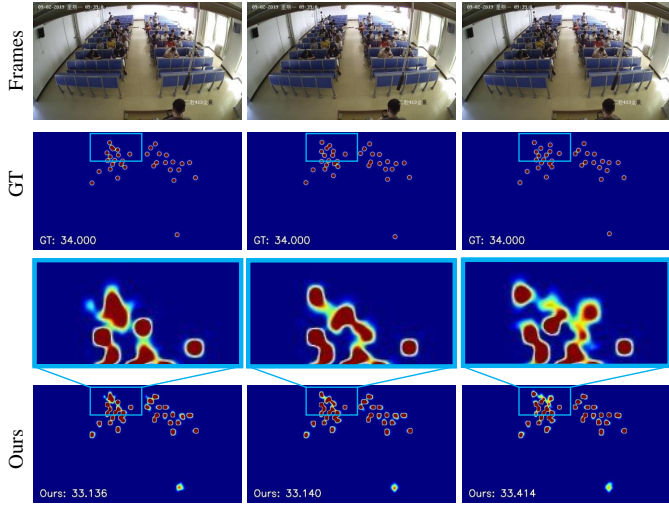


Fig. 11. Visualization of our model across three consecutive frames within the Classroom test set, highlighting the region of interest where the most significant changes in crowd dynamics are observed.

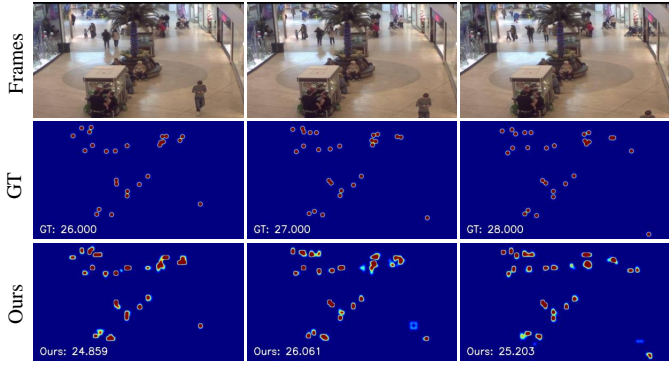


Fig. 12. Visualization of the performance of our model across three consecutive frames on the Mall test set.

in resolutions of either 1920×1080 or 1280×720 . Adhering to the configurations outlined by [20], a total of 60 videos are designated for training purposes, while the remaining 40 videos are reserved for testing.

We evaluate our proposed method against three image-based and three video-based crowd counting approaches in three crowd video datasets, with the results summarized in Table V. As illustrated, our method demonstrates superior performance on the Classroom dataset [25], achieving the lowest MAE and RMSE. Specifically, compared to the second-best performing method, MAF [25], our approach reduces MAE by 6.1% and RMSE by 8.5%. These results indicate that the integration of depth perception alleviates the challenges associated with poor lighting and severe occlusion in indoor environments. Fig. 11 presents a visual representation of the results of our method, displaying three consecutive frames that emphasize dynamic crowd changes, with a particular focus on the most salient regions. Despite movement and variability within the crowd, our method consistently captures these significant dynamic transitions accurately.

Our method does not perform as well on the Mall and FDST datasets as the MAF model [25]. MAF [25] extracts

TABLE VI
EFFICIENCY ANALYSIS OF THE COMPARED METHODS. OURS-W/O-RAFT : WITHOUT THE PRE-TRAINING MODEL OF RAFT.

Method	Type	Parameters(M)	FPS
CSRNet [5]	Image	68.00	>30
CAN [7]	Image	75.02	>30
EPF [22]	Video	78.10	22 ~ 23
STGN [23]	Video	47.35	>30
MAF [25]	Video	250.35	26 ~ 27
Ours-w/o-RAFT	Video	97.50	21 ~ 22
Ours	Video	118.63	8 ~ 9

motion features through bidirectional frame difference and combines these motion features with static features of the current frame for crowd counting. When processing the Mall and FDST datasets, the bidirectional frame difference can more easily eliminate the effects of disturbances because the background and lighting conditions are relatively stable. While, our method still demonstrated notable improvements compared to the EPF model [22]. To visually demonstrate the efficacy of our approach, Fig. 12 illustrates the visualization results on the Mall dataset [49], while Fig. 13 provides the visualization outcomes for both indoor and outdoor scenes from the FDST dataset [20]. These visualizations serve to further substantiate the adaptability and robust performance of our method in various environments.

E. Discussion

1) *Efficiency Analysis:* In practical applications, both model size and operational efficiency serve as critical metrics for evaluating performance. In the Table VI, we summarized the operation efficiency and model size of some comparison methods. The experiment performed operations on images with a size of 640×360 . Generally, the single-image-based approach can meet the real-time requirements. The frame rate of our method can reach more than 20 frames without calculating the pre-training model of RAFT [46]. However, if the pre-training model of RAFT [46] is loaded together with our method, the frame rate is about $8 \sim 9$ frames. Given that in practical counting tasks it is not essential to generate predictions for each frame, the current processing speed is sufficient to meet the requirements of real-world applications. The frame rate of MAF [25] approaches real-time; however, it has the largest number of model parameters, making deployment on edge computing devices challenging. In contrast, while STGN [23] exhibits inferior performance compared to other video counting methods, its smaller number of model parameters and a frame rate exceeding 30 FPS facilitate easier deployment on edge computing devices.

2) *Perspectives of Future Works and Applications:* The limited visibility in underwater environments, combined with the high similarity between foreground and background in terms of appearance, color, and texture, poses significant challenges for distinguishing and accurately counting foreground objects.

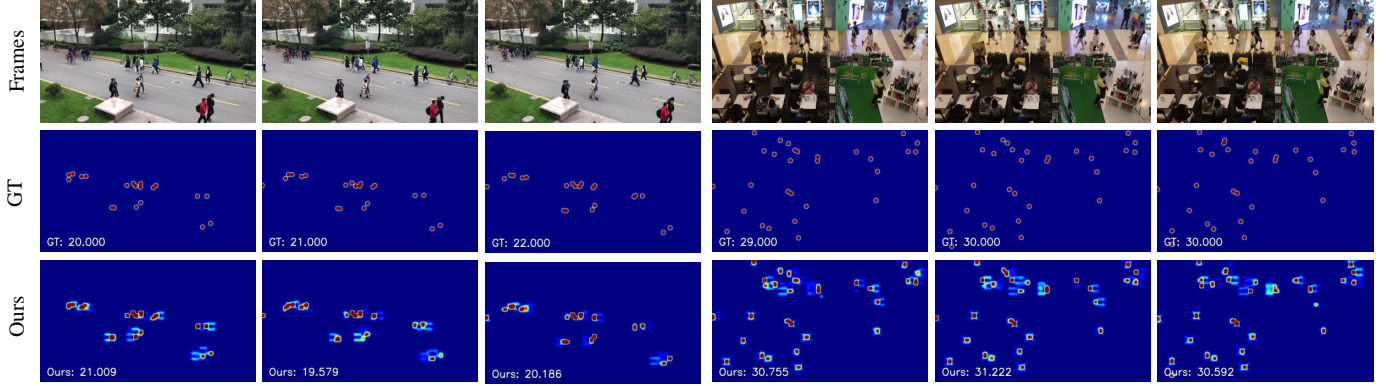


Fig. 13. Visualization of the performance of our model across three consecutive frames in both outdoor and indoor settings on the FDST test set.

Consequently, effective differentiation between foreground and background is crucial for addressing the issue of indiscernible object counting in underwater scenes. Future research should explore the integration of additional information, such as semantics, to enhance feature extraction in regions with indiscernible targets. It holds promise for improving model performance and operational efficiency, thereby facilitating more challenging and complicated downstream applications in real-world scenarios.

V. CONCLUSION

Indiscernible object counting in marine environments has extensive applications in marine resource surveys, ecological monitoring, and fisheries management. Image-based counting methods exhibit notable limitations in capturing spatial and temporal scale information, hindering their ability to satisfy the requirements of practical applications. In contrast, video-based counting is emerging as a promising approach due to its potential capability to address these challenges. In this paper, we propose VIMOC-Net, a depth-assisted network with adaptive motion-differentiated feature encoding for indiscernible marine object video counting. It leverages depth-aware features to enhance the spatial feature representation of indiscernible objects. Meanwhile, adaptive flow estimation on multi-scale perception features is conducted effectively addressing the issue of motion scale variations. The performance of VIMOC-Net has been rigorously validated on both our self-built challenging VIMOC dataset, which comprises 50 videos with approximately 40,800 annotated points, and several widely recognized video crowd counting datasets. Specifically, when evaluated on the VIMOC dataset, VIMOC-Net achieved a reduction in error estimation levels by 10.96% in MAE and 9.8% in RMSE compared to current state-of-the-art methods. In addition, ablation studies highlight the significant contributions of the proposed modules to overall performance.

REFERENCES

- [1] G. Sun, Z. An, Y. Liu, C. Liu, C. Sakaridis, D.-P. Fan, and L. Van Gool, “Indiscernible object counting in underwater scenes,” in *IEEE/CVF Conference on Computer Vision and Pattern Recognition*, 2023, pp. 13 791–13 801.
- [2] K. Li, H. Fan, Q. Qi, C. Yan, K. Sun, and Q. M. J. Wu, “TCTL-Net: Template-free color transfer learning for self-attention driven underwater image enhancement,” *IEEE Transactions on Circuits and Systems for Video Technology*, vol. 34, no. 6, pp. 4682–4697, 2024.
- [3] Q. Qi, K. Li, H. Zheng, X. Gao, G. Hou, and K. Sun, “SGUIE-Net: Semantic attention guided underwater image enhancement with multi-scale perception,” *IEEE Transactions on Image Processing*, vol. 31, pp. 6816–6830, 2022.
- [4] Y. Zhang, D. Zhou, S. Chen, S. Gao, and Y. Ma, “Single-image crowd counting via multi-column convolutional neural network,” in *IEEE/CVF Conference on Computer Vision and Pattern Recognition*, 2016, pp. 589–597.
- [5] Y. Li, X. Zhang, and D. Chen, “CSRNet: Dilated convolutional neural networks for understanding the highly congested scenes,” in *IEEE/CVF Conference on Computer Vision and Pattern Recognition*, 2018, pp. 1091–1100.
- [6] H. Idrees, M. Tayyab, K. Athrey, D. Zhang, S. Al-Maadeed, N. Rajpoot, and M. Shah, “Composition loss for counting, density map estimation and localization in dense crowds,” in *European Conference on Computer Vision*, 2018, pp. 532–546.
- [7] W. Liu, M. Salzmann, and P. Fua, “Context-aware crowd counting,” in *IEEE/CVF Conference on Computer Vision and Pattern Recognition*, 2019, pp. 5099–5108.
- [8] Q. Wang, J. Gao, W. Lin, and X. Li, “NWPU-Crowd: A large-scale benchmark for crowd counting and localization,” *IEEE Transactions on Pattern Analysis and Machine Intelligence*, vol. 43, no. 6, pp. 2141–2149, 2021.
- [9] V. A. Sindagi, R. Yasarla, and V. M. Patel, “JHU-CROWD++: Large-scale crowd counting dataset and a benchmark method,” *IEEE Transactions on Pattern Analysis and Machine Intelligence*, vol. 44, no. 5, pp. 2594–2609, 2022.
- [10] H. Lin, Z. Ma, R. Ji, Y. Wang, and X. Hong, “Boosting crowd counting via multifaceted attention,” in *IEEE/CVF Conference on Computer Vision and Pattern Recognition*, 2022, pp. 19 628–19 637.
- [11] Y. Fan, J. Wan, and A. J. Ma, “Learning crowd scale and distribution for weakly supervised crowd counting and localization,” *IEEE Transactions on Circuits and Systems for Video Technology*, vol. 35, no. 1, pp. 713–727, 2025.
- [12] D. Onoro-Rubio and R. J. López-Sastre, “Towards perspective-free object counting with deep learning,” in *European Conference on Computer Vision*. Springer, 2016, pp. 615–629.
- [13] M.-R. Hsieh, Y.-L. Lin, and W. H. Hsu, “Drone-based object counting by spatially regularized regional proposal network,” in *IEEE/CVF International Conference on Computer Vision*, 2017, pp. 4145–4153.
- [14] Q. Zhao, J. Xiao, Z. Wang, X. Ma, M. Wang, and S. Satoh, “Vehicle counting in very low-resolution aerial images via cross-resolution spatial consistency and intra-resolution time continuity,” *IEEE Transactions on Geoscience and Remote Sensing*, vol. 60, pp. 1–13, 2022.
- [15] Z. Shen, G. Li, R. Xia, H. Meng, and Z. Huang, “A lightweight object counting network based on density map knowledge distillation,” *IEEE Transactions on Circuits and Systems for Video Technology*, vol. 35, no. 2, pp. 1492–1505, 2025.
- [16] H. Lu, Z. Cao, Y. Xiao, B. Zhuang, and C. Shen, “TasselNet: Counting maize tassels in the wild via local counts regression network,” *Plant Methods*, vol. 13, pp. 1–17, 2017.

[17] H. Zheng, X. Fan, W. Bo, X. Yang, T. Tjahjadi, and S. Jin, “A multiscale point-supervised network for counting maize tassels in the wild,” *Plant Phenomics*, vol. 5, p. 0100, 2023.

[18] W. N. C. Veramendi and P. E. Cruvinel, “Method for maize plants counting and crop evaluation based on multispectral images analysis,” *Computers and Electronics in Agriculture*, vol. 216, p. 108470, 2024.

[19] F. Xiong, X. Shi, and D.-Y. Yeung, “Spatiotemporal modeling for crowd counting in videos,” in *IEEE/CVF International Conference on Computer Vision*, 2017, pp. 5151–5159.

[20] Y. Fang, B. Zhan, W. Cai, S. Gao, and B. Hu, “Locality-constrained spatial transformer network for video crowd counting,” in *IEEE International Conference on Multimedia and Expo*, 2019, pp. 814–819.

[21] M. A. Hossain, K. Cannons, D. Jang, F. Cuzzolin, and Z. Xu, “Video-based crowd counting using a multi-scale optical flow pyramid network,” in *Asian Conference on Computer Vision*, 2020.

[22] W. Liu, M. Salzmann, and P. Fua, “Counting people by estimating people flows,” *IEEE Transactions on Pattern Analysis and Machine Intelligence*, vol. 44, no. 11, pp. 8151–8166, 2022.

[23] Z. Wu, X. Zhang, G. Tian, Y. Wang, and Q. Huang, “Spatial-temporal graph network for video crowd counting,” *IEEE Transactions on Circuits and Systems for Video Technology*, vol. 33, no. 1, pp. 228–241, 2023.

[24] Y. Hou, S. Zhang, R. Ma, H. Jia, and X. Xie, “Frame-recurrent video crowd counting,” *IEEE Transactions on Circuits and Systems for Video Technology*, vol. 33, no. 9, pp. 5186–5199, 2023.

[25] M. Ling, T. Pan, Y. Ren, K. Wang, and X. Geng, “Motional foreground attention-based video crowd counting,” *Pattern Recognition*, vol. 144, p. 109891, 2023.

[26] L. Yang, B. Kang, Z. Huang, X. Xu, J. Feng, and H. Zhao, “Depth anything: Unleashing the power of large-scale unlabeled data,” in *IEEE/CVF Conference on Computer Vision and Pattern Recognition*, 2024, pp. 10371–10381.

[27] J. Liu, C. Gao, D. Meng, and A. G. Hauptmann, “DecideNet: Counting varying density crowds through attention guided detection and density estimation,” in *IEEE/CVF Conference on Computer Vision and Pattern Recognition*, 2018, pp. 5197–5206.

[28] Y. Liu, M. Shi, Q. Zhao, and X. Wang, “Point in, box out: Beyond counting persons in crowds,” in *IEEE/CVF Conference on Computer Vision and Pattern Recognition*, 2019, pp. 6469–6478.

[29] D. B. Sam, S. V. Peri, M. N. Sundararaman, A. Kamath, and R. V. Babu, “Locate, size, and count: Accurately resolving people in dense crowds via detection,” *IEEE Transactions on Pattern Analysis and Machine Intelligence*, vol. 43, no. 8, pp. 2739–2751, 2021.

[30] S. Wu and F. Yang, “Boosting detection in crowd analysis via under-utilized output features,” in *IEEE/CVF Conference on Computer Vision and Pattern Recognition*, 2023, pp. 15609–15618.

[31] Q. Song, C. Wang, Z. Jiang, Y. Wang, Y. Tai, C. Wang, J. Li, F. Huang, and Y. Wu, “Rethinking counting and localization in crowds: A purely point-based framework,” in *IEEE/CVF International Conference on Computer Vision*, 2021, pp. 3365–3374.

[32] D. Liang, W. Xu, and X. Bai, “An end-to-end transformer model for crowd localization,” in *European Conference on Computer Vision*. Springer, 2022, pp. 38–54.

[33] T. Han, L. Bai, L. Liu, and W. Ouyang, “STEERER: Resolving scale variations for counting and localization via selective inheritance learning,” in *IEEE/CVF International Conference on Computer Vision*, 2023, pp. 21848–21859.

[34] Y. Ranasinghe, N. G. Nair, W. G. C. Bandara, and V. M. Patel, “CrowdDiff: Multi-hypothesis crowd density estimation using diffusion models,” in *IEEE/CVF Conference on Computer Vision and Pattern Recognition*, 2024, pp. 12809–12819.

[35] Z. Ma, X. Wei, X. Hong, and Y. Gong, “Bayesian loss for crowd count estimation with point supervision,” in *IEEE/CVF International Conference on Computer Vision*, 2019, pp. 6142–6151.

[36] B. Wang, H. Liu, D. Samaras, and M. H. Nguyen, “Distribution matching for crowd counting,” *Advances in Neural Information Processing Systems*, vol. 33, pp. 1595–1607, 2020.

[37] J. Wan, Z. Liu, and A. B. Chan, “A generalized loss function for crowd counting and localization,” in *IEEE/CVF Conference on Computer Vision and Pattern Recognition*, 2021, pp. 1974–1983.

[38] Z. Yan, Y. Qi, G. Li, X. Liu, W. Zhang, M.-H. Yang, and Q. Huang, “Progressive multi-resolution loss for crowd counting,” *IEEE Transactions on Circuits and Systems for Video Technology*, vol. 34, no. 5, pp. 3232–3244, 2024.

[39] M. Jaderberg, K. Simonyan, A. Zisserman *et al.*, “Spatial transformer networks,” *Advances in Neural Information Processing Systems*, vol. 28, 2015.

[40] D. Lian, J. Li, J. Zheng, W. Luo, and S. Gao, “Density map regression guided detection network for rgb-d crowd counting and localization,” in *IEEE/CVF Conference on Computer Vision and Pattern Recognition*, 2019, pp. 1821–1830.

[41] L. Liu, J. Chen, H. Wu, G. Li, C. Li, and L. Lin, “Cross-modal collaborative representation learning and a large-scale rgbt benchmark for crowd counting,” in *IEEE/CVF Conference on Computer Vision and Pattern Recognition*, 2021, pp. 4823–4833.

[42] H. Tang, Y. Wang, and L.-P. Chau, “TAFNet: A three-stream adaptive fusion network for rgbt crowd counting,” in *IEEE International Symposium on Circuits and Systems*, 2022, pp. 3299–3303.

[43] H. Li, J. Zhang, W. Kong, J. Shen, and Y. Shao, “CSA-Net: Cross-modal scale-aware attention-aggregated network for rgbt crowd counting,” *Expert Systems with Applications*, vol. 213, p. 119038, 2023.

[44] H. Meng, X. Hong, C. Wang, M. Shang, and W. Zuo, “Multi-modal crowd counting via a broker modality,” in *European Conference on Computer Vision*. Springer, 2025, pp. 231–250.

[45] K. Simonyan and A. Zisserman, “Very deep convolutional networks for large-scale image recognition,” *arXiv preprint arXiv:1409.1556*, 2014.

[46] Z. Teed and J. Deng, “RAFT: Recurrent all-pairs field transforms for optical flow,” in *European Conference on Computer Vision*. Springer, 2020, pp. 402–419.

[47] D. P. Kingma, “Adam: A method for stochastic optimization,” *arXiv preprint arXiv:1412.6980*, 2014.

[48] W. Zhou, Y. Pan, J. Lei, L. Ye, and L. Yu, “DEFNet: Dual-branch enhanced feature fusion network for rgbt crowd counting,” *IEEE Transactions on Intelligent Transportation Systems*, vol. 23, no. 12, pp. 24540–24549, 2022.

[49] K. Chen, C. C. Loy, S. Gong, and T. Xiang, “Feature mining for localized crowd counting,” in *British Machine Vision Conference*, vol. 1, no. 2, 2012, p. 3.